

## Formation of Piezoelectric Single-Crystal Nanorings and Nanobows

William L. Hughes and Zhong L. Wang\*

Contribution from the School of Materials Science and Engineering and School of Chemistry and Biochemistry, Georgia Institute of Technology, Atlanta, Georgia 30332-0245

Received February 10, 2004; E-mail: zhong.wang@mse.gatech.edu

**Abstract:** Bending of polar-surface-dominated (PSD) nanobelts of ZnO can be explained by one of two processes: electrostatic neutralization of the dipole moment via deformation (called an electrostatic polar charge model) or imbalances between surface tensions via surface-termination induced stresses. This article presents experimental data on the structural features of *nanorings* and *nanobows* formed by bending single-crystal, PSD ZnO nanobelts. Our data exclusively support the electrostatic polar charge model as the dominant mechanism for bending.

### 1. Introduction

Nanobelts of functional oxides were discovered in 2001.<sup>1</sup> Zinc oxide (ZnO), as an important functional oxide, is a semiconducting and piezoelectric material that has practical and scientific importance in the areas of sensing,<sup>2</sup> piezoelectric transduction,<sup>3</sup> surface acoustic wave propagation,<sup>4</sup> and photonics.<sup>5</sup> Scientifically, ZnO is a primary candidate for studying polarization-induced ferroelectricity at the nanoscale,<sup>6,7</sup> piezoelectricity in tetrahedrally coordinated semiconductors,<sup>8</sup> and surface compensating mechanisms for polar surfaces.<sup>9</sup> Structurally, ZnO has a noncentral symmetric Wurtzite crystal structure with a hexagonal Bravais lattice ( $a_0 = 0.325$  nm and  $c_0 = 0.520$  nm). ZnO can be schematically represented as alternating planes of tetrahedrally coordinated  $O^{2-}$  and  $Zn^{2+}$  ions along its  $c$ -axis. The oppositely charged ions produce positively charged Zn–(0001) and negatively charged O–(000 $\bar{1}$ ) polar surfaces, resulting in spontaneous polarization along the  $c$ -axis.

The polar surfaces of ionic crystals exhibit different physical and chemical properties.<sup>10</sup> We have recently observed polar surface-induced anisotropic growth of nanostructures for ZnO,<sup>11</sup> ZnS,<sup>12</sup> and CdSe.<sup>13</sup> In regard to ZnO, Wang et al.<sup>11</sup> have shown

that the Zn-terminated (0001) polar surfaces are chemically active while the O-terminated (000 $\bar{1}$ ) polar surfaces are chemically inert. ZnO has two typical polar surfaces:  $\pm(0001)$  and  $\{01\bar{1}\}$ . These polar surfaces are suggested to be responsible for the formation of seamless nanorings,<sup>6</sup> nanoloops,<sup>7</sup> nanosprings/nanohelicals,<sup>7</sup> deformation-free nanohelices,<sup>20</sup> and nanospirals<sup>14</sup> by rolling up single-crystal ZnO nanobelts.

We have proposed a mechanism for the formation of nanorings.<sup>7</sup> For a thin, straight polar surface-dominated (PSD) nanobelt, the spontaneous polarization-induced electrostatic energy decreases upon rolling into a circular ring due to the neutralization of the dipole moment. However, the elastic energy introduced during deformation increases. If the nanobelt is sufficiently thin ( $<20$  nm), the former can overcome the latter, so that the total energy reduces by forming a ring. The stable shape of the ring is dictated by the minimization of the total energy contributed by spontaneous polarization and elasticity. This is the electrostatic polar charge model.<sup>7</sup>

Alternatively, surface tension is a second possible explanation for the spontaneous bending of PSD single-crystal thin sheets. In early work conducted by Cahn and Hanneman,<sup>15</sup> a theory was presented for explaining the spontaneous bending of thin III–V semiconducting crystals, such as InSb, which has In-terminated (111) and Sb-terminated ( $\bar{1}\bar{1}\bar{1}$ ) surfaces. The model is based on the difference in surface tensions and energies between the In- and Sb-terminated surfaces.

- (1) Pan, Z. W.; Dai, Z. R.; Wang, Z. L. *Science* **2001**, *291*, 1947.
- (2) Hughes, W. L.; Wang, Z. L. *Appl. Phys. Lett.* **2003**, *82*, 2886.
- (3) Minne, S. C.; Manalis, S. R.; Quate, C. F. *Appl. Phys. Lett.* **1995**, *67*, 3918.
- (4) Gorla, C. R.; Emanetoglu, N. W.; Liang, S.; Mayo, W. E.; Lu, Y.; Wraback, M.; Shen, J. *J. Appl. Phys.* **1999**, *85*, 2595.
- (5) Wang, X. D.; Summers, C. J.; Wang, Z. L. *Nano Lett.* **2004**, *3*, 423.
- (6) Kong, X. Y.; Ding, Y.; Yang, R. S.; Wang, Z. L. *Science* **2004**, *303*, 1348.
- (7) Kong, X. Y.; Wang, Z. L. *Nano Lett.* **2003**, *3*, 1625.
- (8) (a) Corso, A. D.; Posternak, M.; Resta, R.; Baldereschi, A. *Phys. Rev. B* **1994**, *50*, 10715. (b) Catti, M.; Noel, Y.; Dovesi, R. *J. Phys. Chem. Solids* **2003**, *64*, 2183.
- (9) (a) Tasker P. W. *J. Phys. C: Solid State Phys.* **1979**, *12*, 4977. (b) Maki, H.; Ichinose, N.; Ohashi, N.; Haneda, H. *Surf. Sci.* **2000**, *457*, 377. (c) Dulub O.; Diebold U.; Kresse G. *Phys. Rev. Lett.* **2003**, *90*, 016102-1. (d) Wander A.; Schedin F.; Steadman P.; Norris A.; McGrath R.; Turner T. S.; Thornton G.; Harrison N. M. *Phys. Rev. Lett.* **2001**, *86*, 3811. (e) Kunat, M.; Girol, S. G.; Becker, T.; Burghaus, U.; Woll, C. *Phys. Rev. B* **2002**, *66*, 081402-1. (f) Overbury, S. H.; Radulovic, P. V.; Thevuthasan, S.; Herman, G. S.; Henerson, M. A.; Peden, C. H. F. *Surf. Sci.* **1998**, *410*, 106. (g) Staemmler, V.; Fink, K.; Meyer, B.; Marx, D.; Kunat, M.; Gil Girol, S.; Burghaus, U.; Woll, Ch. *Phys. Rev. Lett.* **2003**, *90*, 106102-1.
- (10) Vohs, J. M.; Barteau, M. A. *Surf. Sci.* **1986**, *176*, 91.

- (11) Wang, Z. L.; Kong, X. Y.; Zuo, J. M. *Phys. Rev. Lett.* **2003**, *91*, 185502-1.
- (12) Moore, D.; Ronning, C.; Wang, Z. L. *Chem. Phys. Lett.* **2004**, *385*, 8.
- (13) Ma, C.; Ding, Y.; Moore, D.; Wang, X. D.; Wang, Z. L. *J. Am. Chem. Soc.* **2004**, *126*, 708.
- (14) Kong, X. Y.; Wang, Z. L. *Appl. Phys. Lett.* **2004**, *84*, 975.
- (15) Cahn, J. W.; Hanneman, R. E. *Surf. Sci.* **1964**, *1*, 387.
- (16) Gao, P. X.; Wang, Z. L. *Appl. Phys. Lett.* **2004**, *84*, 2883.
- (17) (a) Bai, X. D.; Gao, P. X.; Wang, Z. L.; Wang, E. G. *Appl. Phys. Lett.* **2003**, *82*, 4806. (b) Mao, S.; Zhao, M.; Wang, Z. L. *Appl. Phys. Lett.* **2002**, *83*, 993.
- (18) Bernardini F.; Fiorentini V. *Phys. Rev. B* **1998**, *58*, 15292.
- (19) Bernardini F.; Fiorentini V.; Vanderbilt D. *Phys. Rev. B* **1997**, *56*, 10024.
- (20) Yang, R. S.; Ding, Y.; Wang, Z. L. *Phys. Rev. Lett.* **2004**, submitted.

The objective of this article is to present an experimental study of novel nanostructures that exclusively supports the electrostatic polar charge model as the dominant process in the formation of nanorings,<sup>6</sup> nanobows and nanosprings,<sup>7</sup> and nanohelices.<sup>20</sup> We first present nanorings that are formed by bending PSD nanobelts with a radial direction (originated from the ring center) of  $[0001]$  or  $[000\bar{1}]$ . The inner surface of the rings can be oxygen-terminated ( $000\bar{1}$ ) or Zn-terminated ( $0001$ ). Nonselective bending between the  $\pm[0001]$  supports the polar charge model because the surface tension model requires bending in *only* one specific direction (with the inner surface having less surface tension). We then present novel PSD single-crystal nanobows and their formation process. A model calculation is then presented that predicts the thickness-to-radius ratio of nanorings formed by the spontaneous polar charge model. The results of the calculation are in excellent agreement with the experimental measurements. Finally, we illustrate a PSD, single-crystal, zigzag structure of ZnO, which is caused by fluctuations in growth kinetics and shows the ability of PSD nanobelts to grow along multiple directions.

## 2. Experimental Method

The nanorings and nanobows under investigation were synthesized by thermal evaporation of ZnO powder. Two and a half grams of ZnO powder was used as the source material and placed within the center of a horizontally aligned tube furnace where the temperature, pressure, and evaporation time were manually controlled. The furnace was heated and maintained at a maximum temperature of 1350 °C for 2 h with a pressure of 300 mbar. Argon, with a flux of 50 sccm, was used as a carrier gas throughout the experiment. Upon experimental completion, a vacuum of  $10^{-1}$  mbar was pulled to evacuate the chamber. During evaporation, the products were deposited onto a catalyst-free polycrystalline substrate of alumina that was placed downstream within an alumina tube. The deposition temperature was estimated to be  $\sim 500$  °C. The above experiment has been successfully reproduced in our laboratory.

The as-synthesized samples were first analyzed by a LEO 1530, field emission scanning electron microscope (SEM) at a resolution limit of 1 nm. The thickness-to-radius ratios of 53 individual nanorings and nanobows were measured with an estimated error of  $\pm 2$  nm using an InLens detector. Individual radii were measured between the imaginary center point of each loop and the middle of each loop at the maximum distance from the ring's center. Assuming perfect loops, this technique eliminated any artifacts caused by the loop not being perpendicular to the viewing direction. For similar reasons, the thickness of each loop was measured at the thinnest location. The samples were then investigated by a JEOL 100C transmission electron microscope (TEM) at 100 kV.

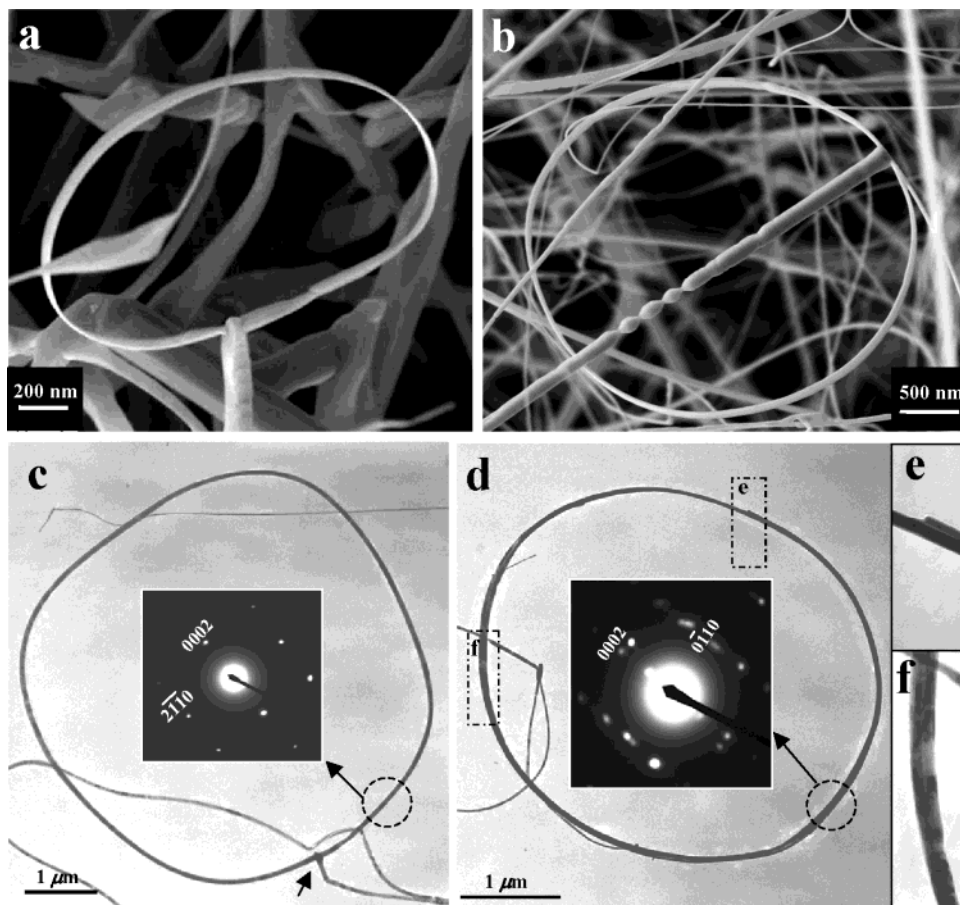
As a complementary study, a third experiment was performed to investigate the effects of growth time on yield and dimensionality of the nanorings and nanobows. In comparison to the experimental method listed above, 10 grams of ZnO was maintained at a maximum temperature of 1350 °C for 10 h. Observationally, the yield and dimensionality of the nanorings and nanobows was comparable for all three experiments. Therefore, reproducibility has been shown for different growth times, even though precise dimensional control of the thickness, width, and radius of the nanostructures has not been investigated. However, dimensional control is envisioned by (1) catalytic control of the size and distribution of the ZnO nanorods that are responsible for sprouting nanorings and nanobows, (2) alignment of ZnO nanorods via single-crystal substrates, and (3) evacuation pressure control at the end of synthesis.

## 3. Experimental Results

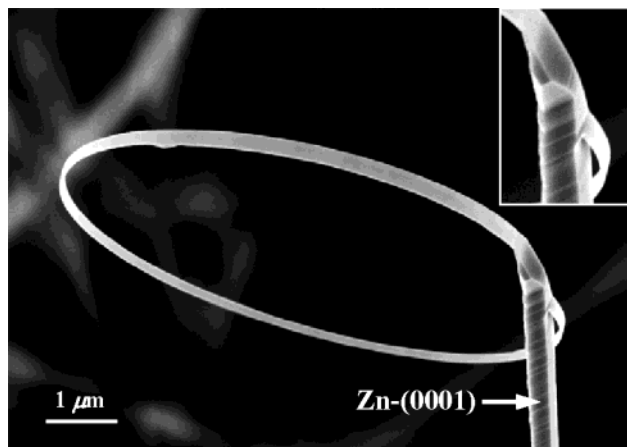
**3.1. Nanorings.** Single rings of ZnO (nanorings) were synthesized using the aforementioned procedure. Nanoring yield was estimated at  $\sim 5\%$  of the total product deposited on the sample substrate. Instead of showing the distribution of rings, the following presentation focuses on the model responsible for ring formation. Examples of two distinct but characteristic nanorings observed with SEM are shown in Figure 1a,b. These images illustrate a nanobelt's unique ability to bend upon itself to form a complete looped ring. Observationally, the radii are much greater than their respective thicknesses, and the widths are significantly larger than their thicknesses. It is known that the rods of ZnO grow along  $[0001]$  and the Zn-terminated surface is at the growth front because of its self-catalysis effect for leading the growth.<sup>11</sup> It is worth noting that regardless of the nanoring's growth direction, the  $\pm c$ -axis is orthogonal to the large flat surface of the ZnO nanobelt and *always* points toward the center of the ring. Combining TEM images of individual nanorings with their corresponding diffraction data confirms this hypothesis. For example, diffraction patterns taken from the enclosed circles in Figure 1c,d shows that the  $c$ -axis points toward the center of the rings while the tangential directions of the individual nanorings are  $[2\bar{1}10]$  and  $[0\bar{1}10]$ , respectively. *Therefore, the nanorings under investigation are polar surface-dominated.* As highlighted with an arrowhead, Figure 1c shows a nanoring that begins and ends from a specific point, while Figure 1d is a nanoring formed by making a successive loop upon itself. An enlarged image of the overlapping ends of the loop is shown in Figure 1e. The tail of the loop is composed of a Zn-terminated surface in physical contact with an O-terminated surface, similar to the formation of an in-plane spiral.<sup>14</sup> As presented by the diffraction contrast image in Figure 1f, bending to form rings introduces a fairly uniform strain.

Figure 2 is a minority nanoring configuration. This image illustrates the remarkable desire for ZnO nanorings to form closed structures. The ZnO rod has a rectangular cross section and a thick ribbon shape (different from the shape of the ZnO nanorods shown in Figure 1a,b, which are hexagonally shaped rods). On the basis of previous studies, the roughened basal-plane surface of the ZnO rod is Zn-terminated, while the smooth basal-plane surface is O-terminated.<sup>16</sup>

**3.2. Nanobows.** Nanobows are novel nanostructures found within this study. Continuous and uniform bending of nanobelts into semirings is characteristic of all nanobows. Typical SEM images of nanobows are shown in Figure 3. When comparing nanorings with nanobows, it is important to refer back to Figure 1b and realize that the nanobows are semicircular. Figure 3a shows a hexagonal ZnO rod with a ZnO nanobelt grown from one of its six primary crystallographic facets. The rod grows along  $[0001]$  with side surfaces of  $\{2\bar{1}10\}$  or  $\{0\bar{1}10\}$ . On the basis of growth of self-catalyzed ZnO nanostructures,<sup>11</sup> the inner arc of the nanobow is believed to be O-terminated while the outer surface is Zn-terminated. Figure 3b illustrates the ability of nanobows to grow along multiple facets of a hexagonal ZnO rod because of their crystallographic equivalence. The two nanobows shown are crystallographically separated by  $180^\circ$ . Figure 3c shows two nanobelts attached to one another prior to joining the hexagonal rod. These two nanobows are  $120^\circ$  apart and exhibit opposite inner and outer surface terminations. Such



**Figure 1.** ZnO nanorings made from individual polar surface-dominated single-crystal nanobelts. (a,b) SEM images showing the geometry of various types of nanorings. (c,d) TEM images and the corresponding electron diffraction patterns showing the geometry and crystallographic structure of nanorings. (e) TEM image showing overlap between successive loops of a Zn- and O-terminated surfaces. Physical contact occurs between the polar surfaces of opposite charge. (f) TEM image showing the uniform strain found within a nanoring.



**Figure 2.** SEM image of a minority single-crystal ZnO nanoring configuration. The rough surface of the rod is believed to be Zn-terminated (0001), and the inner surface of the nanoring is Zn-(0001).

assumptions are based on the single-crystal nature of nanobows (to be presented in Figure 4) and the joining of the nanobows at a common intersecting point. As illustrated by a schematic model (see the inset), the outside faces of the top and bottom nanobows have Zn-terminated (0001) and O-terminated (000 $\bar{1}$ ) surfaces, respectively. At the junction between the two nanobows, the negative inner surface of the top nanobow corresponds to the negative outer surface of the bottom nanobow. As a supplementary example, Figure 3d,e shows a pair of nanobows

growing out of a single nanorod. This structure is likely to have the same sign convention illustrated in Figure 3c.

Figure 4 is a series of TEM images of two types of ZnO nanobows showing their single-crystal structures. Figure 4a shows a junction between a ZnO rod and a ZnO nanobelt. The single-crystal nature of the nanobow is confirmed by electron diffraction patterns recorded from the nanobelt and nanorod junctions. The nanorod grows along [0001] with side surfaces of {01 $\bar{1}$ 0}. The nanobelt grows out of [01 $\bar{1}$ 0] with top/bottom surfaces (0001)/(000 $\bar{1}$ ) and side surfaces  $\pm(2\bar{1}\bar{1}0)$ . As shown for nanorings, the polar surface of the nanobelt is pointing toward the rings center. Figure 4b is a magnified image of the top junction, illustrating a 90° change in growth direction of a single crystal.

Figure 4c is an alternative case of a nanobelt growing along [2 $\bar{1}\bar{1}$ 0], with top/bottom surfaces (0001)/(000 $\bar{1}$ ) and side surfaces  $\pm(01\bar{1}0)$ . As indicated by the electron diffraction pattern, the entire structure is a single crystal (circled region 1). However, the nanobelt twisted itself a short distance away from the junction so that the electron beam was perpendicular to its top surface (see the diffraction pattern from circle 2). The small size of the nanobelt makes such a large twist possible.

A common feature shown in the two cases presented in Figure 4 is that the polar surface *always* points toward the nanobow center. Our analysis confirms a single-crystal structure between the nanobelt and the nanorod. If the nanobelt is without twist,

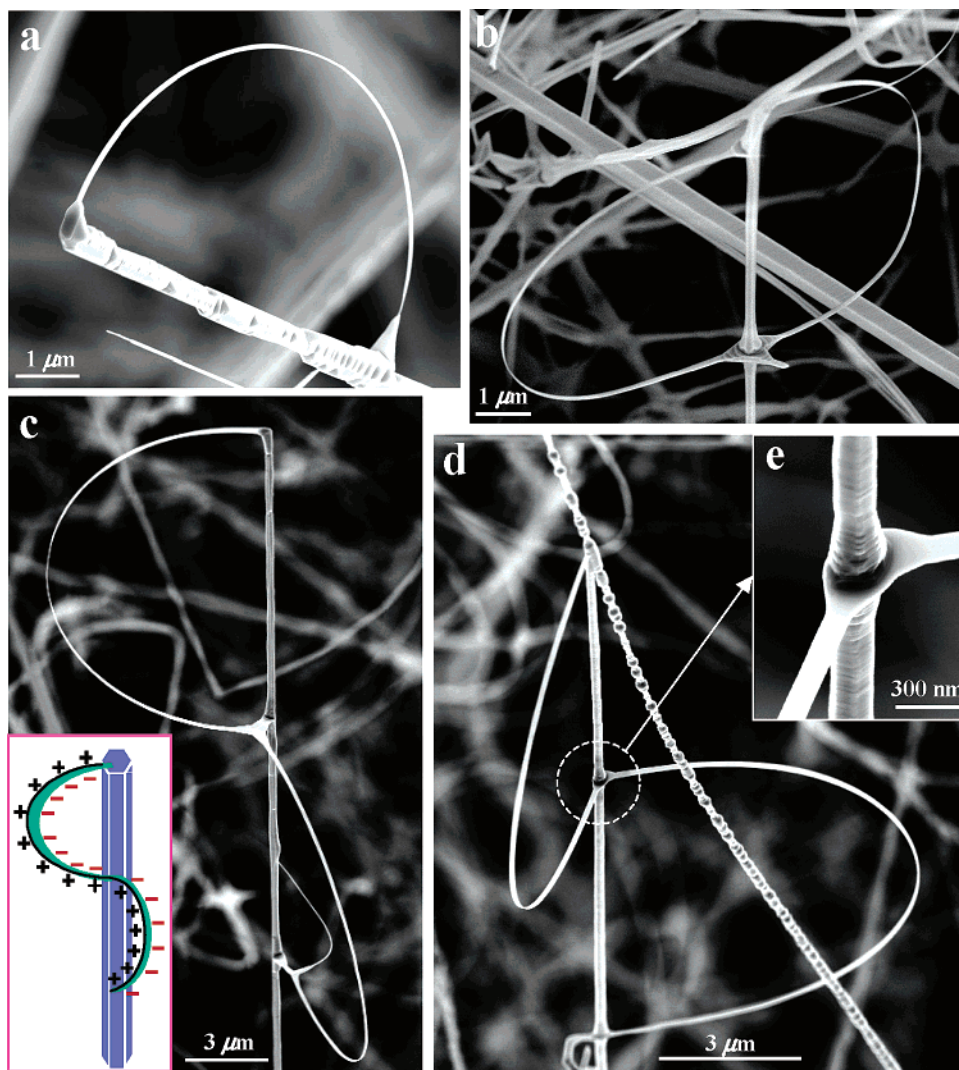


**Figure 3.** ZnO nanobows made from individual polar surface-dominated single-crystal nanobelts. A collection of typical geometrical shapes of the nanobows are presented. A model for the nanobow shown in (c) is inserted, showing their geometry and charge distribution along their polar surfaces (see text for details).

it will bend spontaneously during growth until it directly hits the same crystallographic facet of the nanorod from which it began. Alternatively, if there is a small twist, the nanobelt could bypass the nanorod and reach its starting point in order to form a complete ring.

**3.3. Electrostatic Polar Charge Model versus Surface Tension Model.** In the surface tension model proposed by Cahn and Hanneman,<sup>15</sup> a key requirement for bending is different surface tensions on opposite faces. The bending is without directional freedom and is toward a specific crystallographic direction. For the nanoring shown in Figure 1a, the inner surface is Zn-terminated (0001) and the outer surface is O-terminated (000 $\bar{1}$ ). Alternatively, for the nanoring shown in Figure 1b, the inner surface is O-terminated (000 $\bar{1}$ ) and the outer surface is Zn-terminated (0001). Also, for the paired nanobows shown in Figure 4c the inner surfaces were oppositely terminated. These results are in stark contrast to the surface tension model and therefore cannot be used to explain the formation of nanorings or nanobows.

In the electrostatic polar charge model, bending is identical and equally probable for  $\pm[0001]$ . The model also prefers closed rings because of geometric neutralization of the dipole moment.

These expected results are consistent with the experimental data presented in section 3. Therefore, the dominant mechanism for bending is the electrostatic polar charge model proposed by Kong and Wang.<sup>7</sup> Using this model, we now calculate the energetically favorable geometrical parameters to compare with experiment.

A dipole moment exists across the thickness of PSD nanobelts.<sup>7</sup> The dipole moment diverges for long, straight nanobelts, while being neutralized by symmetric charge distribution in nanobelt rings. As a result of bending, the electrostatic energy of the entire system is expected to decrease. To begin our calculation, a PSD nanobelt is approximated as small capacitive plates with opposite charges on the top and bottom surfaces. Changes in the electrostatic energy are measured between a flat planar capacitive configuration (length  $L$ , width  $W$ , and thickness  $t$ ) and a cylindrical capacitive configuration (inner radius  $R_1$ , outer radius  $R_2$ , and mean radius  $R = (R_1 + R_2)/2$ ). Assumptions made in regard to nanobelts are (1) nanobelt thickness ( $t$ ) is much smaller than the nanorings diameter ( $R$ ), and (2) the surface charge density ( $s$ ) is preserved between the capacitive plate and capacitive cylinder configurations because the charges are bound to the crystallographic position of the atomic cores.

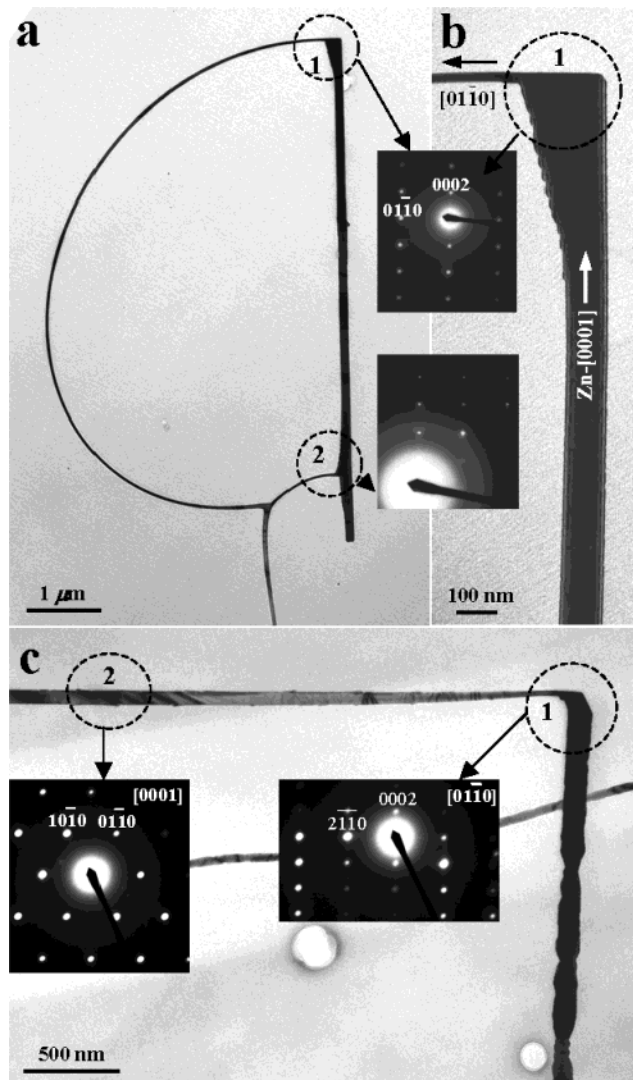


**Figure 4.** TEM images and their corresponding electron diffraction patterns showing the geometry and crystallographic structure of ZnO nanobows. (a,b) Nanobow shows a single crystal junction between a polar surface-dominated nanobelt and a nanorod. The change in growth direction from the nanorod to the nanobelt is 90°, and the nanobelt's polar surface points towards the center of the nanobow. (c) A single-crystal junction between a twisted nanobelt and a nanobow.

Therefore, considering the compression on the inner surface of the nanoring, the total charge on the inner surface of the cylinder is  $Q = 2\pi(R - t/2)W\sigma$ . The width ( $W$ ) of the nanobelt is significantly larger than its thickness, and thus the edge effect is small. However, it is the difference between the electrostatic energy before and after rolling into a cylinder that matters in the final result; if the edge effect before and after rolling is preserved, the edge effect, if any, is almost canceled out in the final equation. Finally, the change in electrostatic energy after rolling a flat nanobelt into a nanoring is given by:

$$\Delta E_{\text{electro}} = \frac{\pi W \sigma^2 R^2}{\epsilon \epsilon_0} \left[ (1 - \beta)^2 \ln \left( \frac{1 + \beta}{1 - \beta} \right) - 2\beta \right] \approx - \left( \frac{\pi W \sigma^2}{\epsilon \epsilon_0} \right) t^2 \quad (1)$$

where  $\beta = t/2R$  and  $\epsilon$  is the dielectric constant of ZnO.

On the other hand, the elastic deformation from forming a ring must be taken into account, which can be calculated using linear elastic theory. Since the thickness of the nanobelt is very

small and the ring radius is large, the radial stress across the nanobelt is negligible because the two sides are free surfaces without external force. The strain along the  $z$ -direction (the axis of the cylinder) is also zero because there is little twisting. The only strain is along the  $\phi$ -direction. The elastic energy is the volume integration of the  $\phi$ -direction strain energy. The bending modulus used for the calculation was based on the experimentally measured value for ZnO nanobelts with inclusion of a geometrical factor. The change in elastic energy is

$$\Delta E_{\text{elastic}} \approx \left( \frac{\pi W Y}{24R} \right) t^3 \quad (2)$$

where  $Y$  is the bending modulus. Therefore, the total change in energy after forming a ring is

$$\Delta E \approx - \left( \frac{\pi W \sigma^2}{\epsilon \epsilon_0} \right) t^2 + \left( \frac{\pi W Y}{24R} \right) t^3 \quad (3)$$

The maximum thickness-to-radius ratio  $(t/R)^*$  is an energetic boundary separating the region between energetically favorable and unfavorable configurations and can be calculated by setting  $\Delta E = 0$ . Thickness-to-radius values less than  $(t/R)^*$  are energetically favorable while values greater than  $(t/R)^*$  are energetically unfavorable. The most energetically favorable thickness-to-radius ratio  $(t/R)_o$  corresponds to the minimum of  $\Delta E$ . The respective equations for  $(t/R)^*$  and  $(t/R)_o$  are:

$$\left( \frac{t}{R} \right)^* = \left( \frac{24\sigma^2}{\epsilon \epsilon_0 Y} \right); \quad \left( \frac{t}{R} \right)_o = \left( \frac{16\sigma^2}{\epsilon \epsilon_0 Y} \right) \quad (4)$$

Using the published data for the values of the bending modulus, dielectric constant, and surface charge density, ( $Y = 50 \pm 5$  GPa,<sup>17</sup>  $\epsilon = 4.6$ ,<sup>18</sup> and  $|\sigma| = 0.057$  C/m<sup>2</sup><sup>19</sup>) we have  $(t/R)^* = (3.8 \pm 0.2) \times 10^{-2}$  and  $(t/R)_o = (2.6 \pm 0.2) \times 10^{-2}$ .

A plot of the thickness-to-radius ratio for single-crystal nanorings of ZnO is shown below in Figure 5a. The red line  $[(t/R)^*]$  divides the plot into a red region that is energetically unfavorable and a green region that is energetically favorable. The black line represents the most energetically favorable  $(t/R)_o$ . The experimentally measured  $(t/R)$  ratio for 53 nanorings and nanobows are plotted, and their linear fit is represented by a blue line. Remarkably, all the experimental values are located within the energetically favorable zone when the error associated with the measurement is accounted for ( $\pm 2$  nm).

Further more, the slope of the  $(t/R)_o$  line does not fit with the slope of the experimental data. A reasonable explanation for the shift in slope is that the surface charge density used in our calculation was adopted from theoretical work and may overestimate the surface charge without considering charge compensation in practical experiments. Doping, surface adsorption, reconstruction, relaxation, and charge transfer can reduce surface charge density. Using the slope of the experimental data, we derived the surface charge density on a real surface of ZnO (0001) to be  $|\sigma| = (0.022 \pm 0.002)$  C/m<sup>2</sup>. When the best fit line was forced to go through the origin, the surface charge density was derived to be  $|\sigma| = (0.027 \pm 0.002)$  C/m<sup>2</sup>. This value is  $\sim 47\%$  of the theoretical value.<sup>19</sup>

It is worth noting that pure ZnO powder was used during synthesis. In prior experiments high resolution TEM confirmed the absence of contamination (unless doping was intentional).

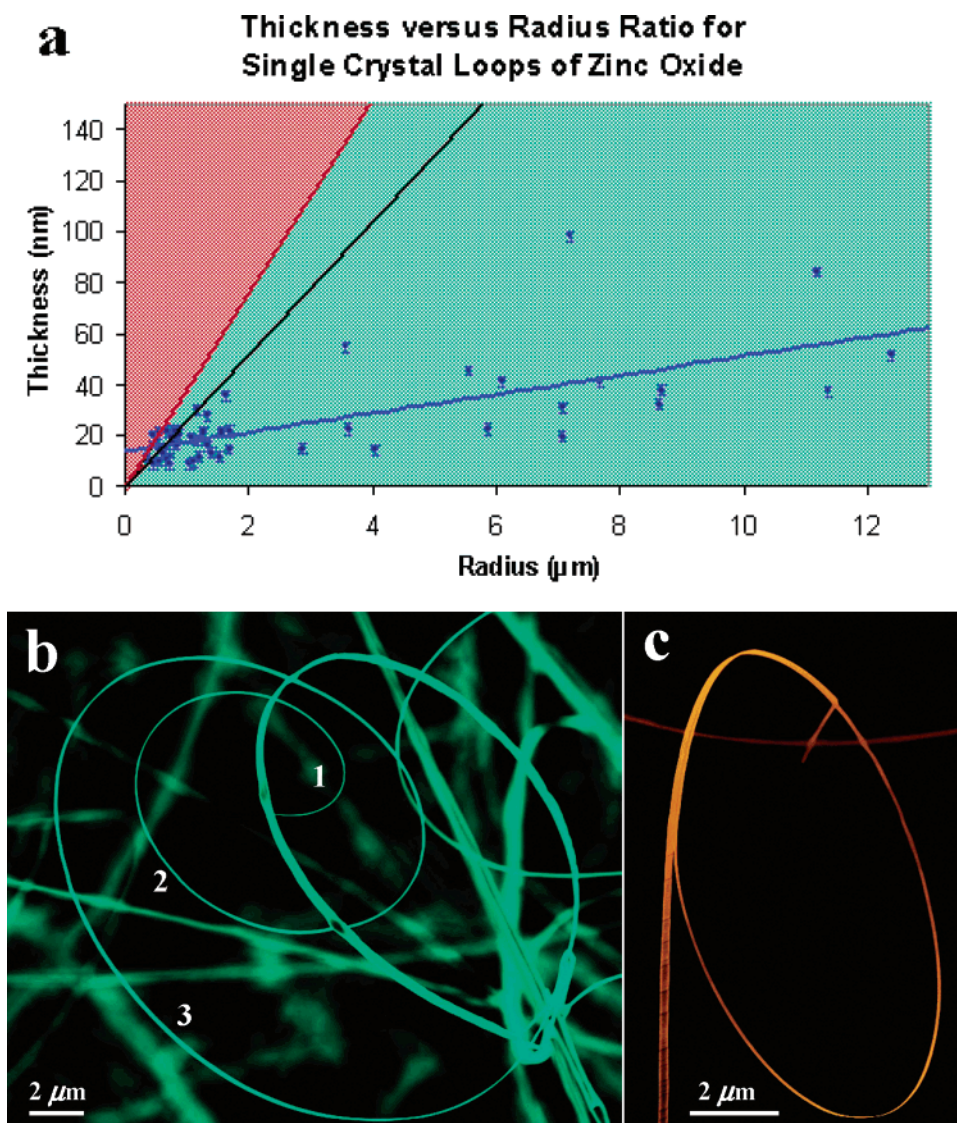


**Figure 5.** (a) Plot showing the thickness-to-radius ratio for single-crystal loops of ZnO. The red and green represent energetically unfavorable and energetically favorable regions. The red line is the critical  $(t/R)^*$  ratio, the black line is the most energetically favorable  $(t/R)_0$  ratio, and the blue line is the experimental fit for rings of known radius and thickness. (b,c) Nanorings showing a change in the radius-of-curvature with a corresponding change in nanobelt thickness.

In addition, the temperature at which ZnO nanorings and nanobows are formed is above that at which physical adsorption can occur. Once the product is removed from the furnace, nanobelt relaxation can occur in the radial direction if the nanobelts are not chemically bonded at two ends. However, all measurements were made on nanorings and nanobows that were chemically bound to form complete rings. Therefore, measurement of the thickness-to-radius ratio should be a reasonable experimental technique for determining the surface charge density for PSD nanobelts. In addition, PSD nanobelts are a primary structure for studying the effects of surface reconstruction, relaxation, and charge transfer.

From eq 4, the radius of the nanoring should increase as the thickness increases. The results shown in Figure 5b,c provide experimental support. Figure 5b shows a single nanobelt coiling to form a spiral. As the thickness of the spiral increases between regions 1 and 3, the radius-of-curvature increases. As a second example, Figure 5c shows a nanoring formed at the end of a nanobelt where the thickness of the nanobelt in the ring region is significantly smaller than that of the nanobelt in the straight

segment. These examples are physical illustrations that as the thickness of the nanobelt is increased, the elastic energy required to bend the nanobelt increases drastically. The nanorings and nanobows are observed only for thin PSD nanobelts.

**3.4. The  $c$ -Plane Dominated Zigzag Structure.** Polar nanobelt growth in Figure 1c,d is along either the  $[2\bar{1}\bar{1}0]$  or  $[01\bar{1}0]$  directions for the formation of nanorings and nanobows. The three dominant growth directions for ZnO nanobelts are  $\langle 0001 \rangle$ ,  $\langle 01\bar{1}0 \rangle$ , and  $\langle 2\bar{1}\bar{1}0 \rangle$ . Nanorings and nanobows are only formed in nanobelts that have large  $\pm(0001)$  polar surfaces. Because of small differences in surface energy between  $\{2\bar{1}\bar{1}0\}$  and  $\{01\bar{1}0\}$ , a small change in growth kinetics can change the growth direction from  $[2\bar{1}\bar{1}0]$  to  $[01\bar{1}0]$  and vice versa. Figure 6a is an example of a PSD nanobelt that has shifted its growth direction. From the diffraction pattern, the zigzag nanobelt is a single crystal with its top/bottom surfaces represented by the large  $(0001)/(000\bar{1})$  polar surfaces. The nanobelt growth direction alternates between the  $[11\bar{2}0] \rightarrow [01\bar{1}0] \rightarrow [\bar{1}2\bar{1}0]$ . It is important to note that the  $[11\bar{2}0]$  and  $[\bar{1}2\bar{1}0]$  are crystallographic equivalent directions.

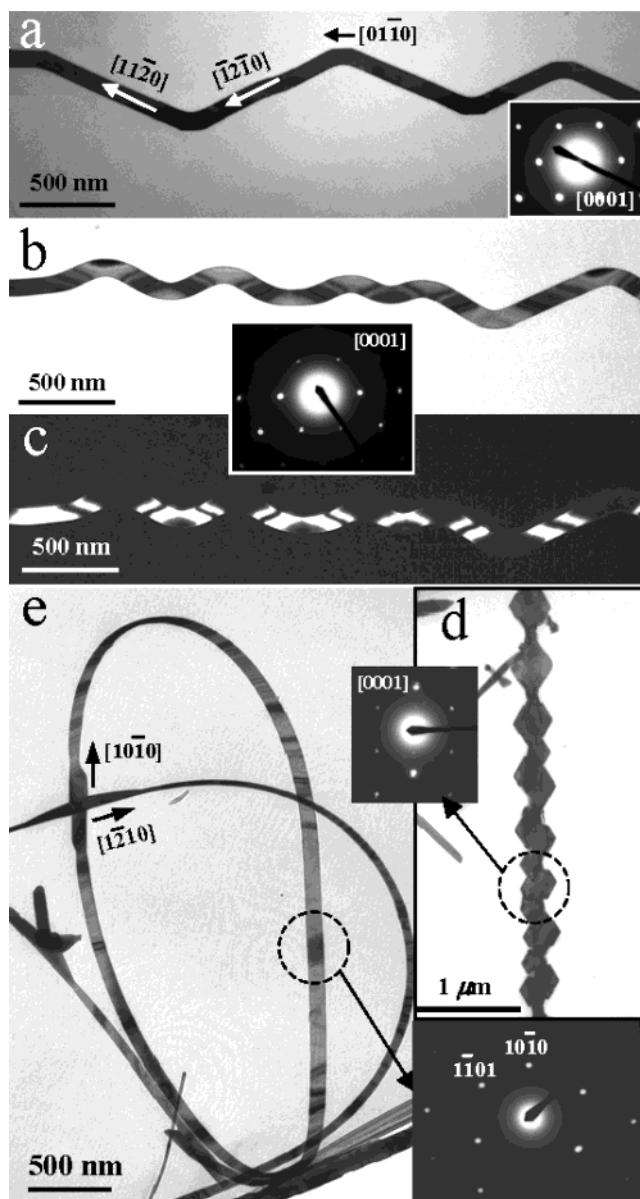


**Figure 6.** TEM images and their corresponding electron diffraction patterns for polar surface-dominated ZnO nanostructures with multiple growth directions. Changes in the growth directions are directly related to changes in the growth kinetics. (a,b) Single-crystal zig-zag, polar surface-dominated nanobelts alternating between their  $[11\bar{2}0] \rightarrow [01\bar{1}0] \rightarrow [\bar{1}2\bar{1}0]$  directions. (c) Dark-field image showing periodic contrast and therefore periodic strain within a polar surface-dominated nanobelt. (d) Single-crystal platelets of polar surface-dominated ZnO showing extreme switching in growth directions. (e) An example of two nanorings growing from the same junction and having two different growth directions.

As a second example, Figure 6b,c is the bright-field and dark-field TEM images from a zigzag nanobelt that has changed its growth direction with greater frequency. As seen from the dark-field image, the bending pattern and strain distribution in each cycle of the zigzag oscillation is similar. Once again the top/

bottom surfaces are the large  $(0001)/(000\bar{1})$  polar surface, while the growth direction alternates between  $[11\bar{2}0] \rightarrow [01\bar{1}0] \rightarrow [\bar{1}2\bar{1}0]$ . Figure 6d is an extreme example of alternating growth directions, where a single crystal of ZnO has formed a series of flat  $(0001)$  platelets. As a final example, Figure 6e shows two nanorings growing orthogonal from one intersection. At the intersection, two single-crystal, PSD nanobelts have grown to make nanorings with respective growth directions of  $[10\bar{1}0]$  and  $[\bar{1}2\bar{1}0]$ .

#### 4. Summary and Conclusion

It is well-known that ZnO is a piezoelectric and semiconducting material. The nanorings and nanobows of single-crystal ZnO presented here are ideal candidates for applications in nanoscale sensors, transducers, and electromechanical coupling devices and converters. In this article, we have reported the growth of PSD nanobelts into piezoelectric nanorings and nanobows of single-crystal ZnO. The nanorings and nanobows are formed by bending PSD nanobelts with a radial direction (originated from the ring center) of  $[0001]$  or  $[000\bar{1}]$ . The inner surfaces of the nanorings and nanobows have been shown to terminate with either O or Zn. The resulting nonselective bending direction between  $[0001]$  and  $[000\bar{1}]$  exclusively supports the electrostatic polar charge model proposed by Kong and Wang.<sup>7</sup> Under this model, deformation of nanobelts into nanorings and nanobows is driven by the minimization of the electrostatic energy produced by polar charges. In comparison, the surface tension model<sup>15</sup> requires bending toward one specific crystallographic direction, with the inside surface containing the smaller of the two surface tension values. Therefore, the surface tension model cannot be supported by our data.

On the basis of the electrostatic polar charge model, we have calculated the theoretically expected thickness-to-radius ratio for nanorings formed by bending polar nanobelts. The results are in excellent agreement with experimental measurements. Using the experimental data, we have derived a surface charge density of  $|\sigma| = (0.02 \text{ to } 0.029) \text{ C/m}^2$  on the ZnO  $\pm(0001)$  surfaces. This demonstrates an experimental approach for measuring the surface charge density on nanobelt polar surfaces. Finally, we illustrated that oscillation of the growth kinetics of PSD nanobelts can result in the formation of single-crystal zigzag structures of ZnO.

**Acknowledgment.** This work was supported by NSF (DMR-9733160) and NASA Vehicle Systems Program and Department of Defense Research and Engineering (DDR&E). Will Hughes gratefully acknowledges partial support from the Georgia Tech Molecular Design Institute, under prime Contract N00014-95-1-1116 from the Office of Naval Research. Thanks to Dr. X. Y. Kong, Puxian Gao, and Brent Buchine for many stimulating discussions.

JA049266M